Supplementary Materials

Nanoporous amorphous carbon nanopillars with lightweight, near-theoretical strength, large fracture strain, and high damping capability

Zhongyuan Li[1,*], Ayush Bhardwaj[2,*], Jinlong He[3], Wenxin Zhang[4], Thomas T. Tran[4], Ying Li[3], Andrew McClung[6], Sravya Nuguri[2], James J. Watkins[2§], Seok-Woo Lee[1§]

1. *Department of Materials Science and Engineering & Institute of Materials Science, University of Connecticut, 25 King Hill Road, Storrs CT 06269-3136, United States*
2. *Department of Polymer Science and Engineering, University of Massachusetts Amherst, 120 Governors Drive, Amherst, MA 01003, United States*
3. *Department of Mechanical Engineering, University of Wisconsin-Madison, 1513 University Ave, Madison, WI 53706, United States*
4. *Division of Engineering and Applied Sciences, California Institute of Technology, 1200 E. California Blvd, Pasadena, CA 91125, United States*
5. *Department of Electrical and Computer Engineering, University of Massachusetts Amherst, , 100 Natural Resources Rd, Amherst, MA 01003, United States*

*Equal Contribution: Zhongyuan Li, Ayush Bhardwaj

§Corresponding Author: James J. Watkins (watkins@polysci.umass.edu),

Seok-Woo Lee (seok-woo.lee@uconn.edu)

1. Porosity and density measurement

Density of the fully dense carbon film was estimated using pycnometer of volume 50 ml. Solid carbon films were floated in the liquid of known densities. Liquid used were 1,2 Dichlorobenzene (1.3 gm/ml) and bromobenzene (1.49 g/ml). The density of carbon is calculated to be 1.62 g/ml**.** This method could not be extended to the nanoporous carbon as their density is very low and liquid with densities lower than these films have very volatility resulting in the error in the measurement. So, Porosity of the nanoporous carbon material was determined using the ellipsometry by utilizing the Bruggeman effective model. `Refractive index as function of wavelength was obtained by fitting the raw data with Si with absorbing film (mean square error < 5) as shown in the Figure S1. The refractive index at 633 nm was used for the porosity calculation using the following equation which correlates the refractive index of the material with the porosity[1]:

$$1-\phi=\frac{\frac{n_{eff}^2}{n_c^2}-\frac{n_d^2}{n_c^2}}{\left[\frac{n_{eff}^2}{n_c^2}\right]^{\frac{1}{3}}\left[1-\frac{n_d^2}{n_c^2}\right]}$$

where, ϕ is the porosity, n_{eff} is the refractive index of investigated nanoporous material, n_c is the refractive index of air/void ~1, n_d is the refractive index of dense carbon film at 633 nm. Based on porosity value obtained from above equation with known density of dense carbon film, density of nanoporous carbon material was calculated which is summarized in Table S1.

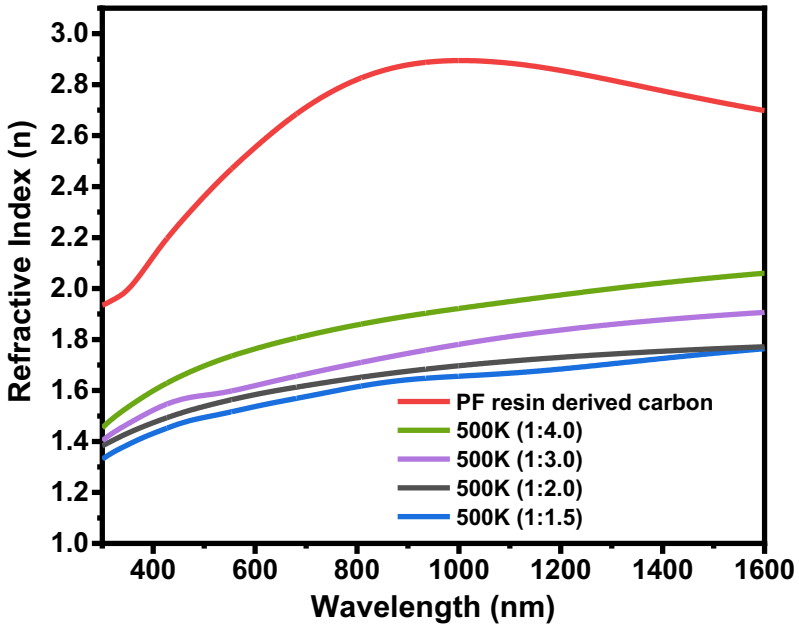

Figure S1. Refractive index as function of wavelength of nanoporous carbon obtained with different loading of carbon precursor.

Sample ID	Porosity	Density (gm/ml)
Carbon	-	1.62
1:1.5	59%	0.66
1:2.0	51%	0.79
1:3.0	46%	0.87
1:4.0	40%	0.97

Table S1. Density of carbon material with different porosity.

2. Microcompression data of nanoimprinted nanopillars

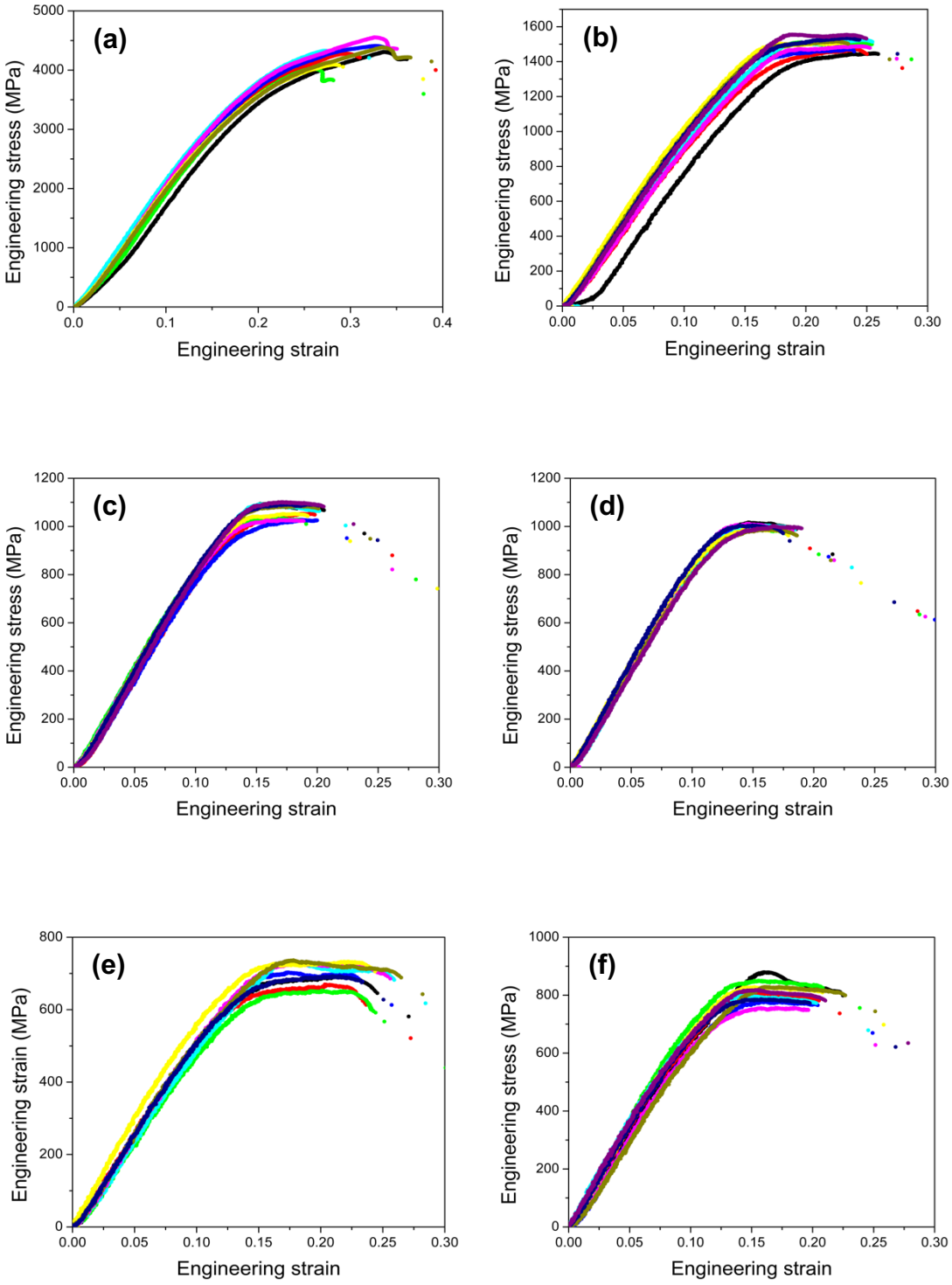

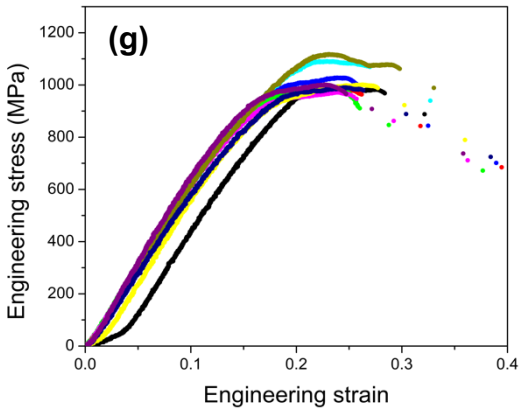

Figure S2. Stress-strain curves of (a) full dense, (b) 40% of porosity, (c) 46% of porosity, (d) 51% of porosity, and (e) 59% of porosity nanopillars. (f) 51% of porosity with small pore size (g) 51% of porosity with large pore size. All data are reproducible, so the errors in mechanical data are very small.

Porosity (%)	Yield strength (MPa)	Fracture strength (MPa)	Fracture strain
0	3121.68 ± 158.14	4198.53 ± 169.25	0.3208 ± 0.0346
40	1121.51 ± 66.64	1489.82 ± 30.94	0.2473 ± 0.0083
46	951.96 ± 47.30	1052.15 ± 23.66	0.1985 ± 0.0056
51	923.64 ± 28.39	978.32 ± 9.81	0.1818 ± 0.0045
59	492.07 ± 55.80	665.71 ± 38.00	0.2456 ± 0.0113
51 (small pore size)	634.15 ± 28.98	787.88 ± 22.83	0.2096 ± 0.0093
51 (large pore size)	797.22 ± 27.65	985.63 ± 44.28	0.2679 ± 0.0140

Table S2. Summary of microcompression data of nanoimprinted nanopillars

2. Nanoindentation data of thin film

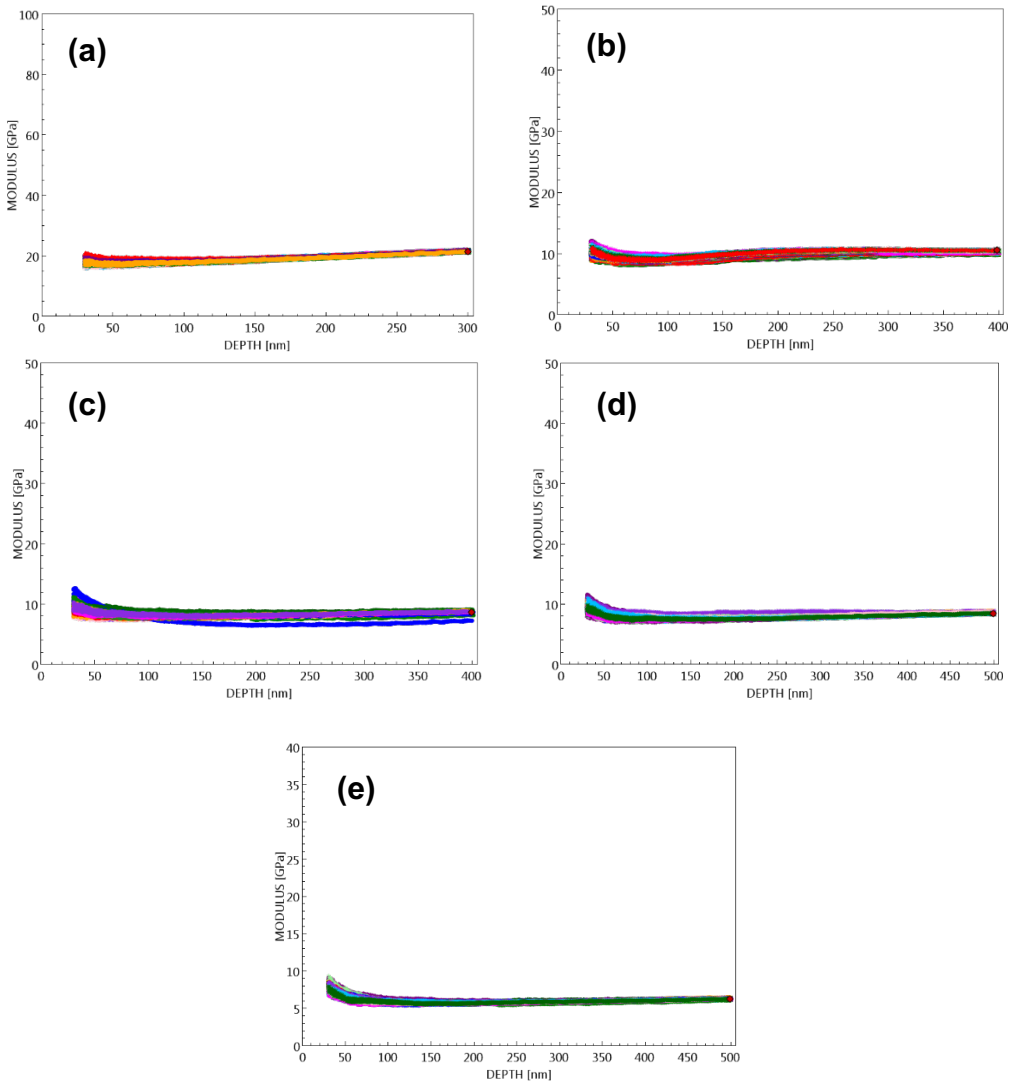

Figure S3. Modulus-depth curves of (a) full dense, (b) 40% of porosity, (c) 46% of porosity, (d) 51% of porosity, and (e) 59% of porosity thin film. Young's modulus data are relatively insensitive to depth, implying that there are no errors related to sink-in or pile-up.

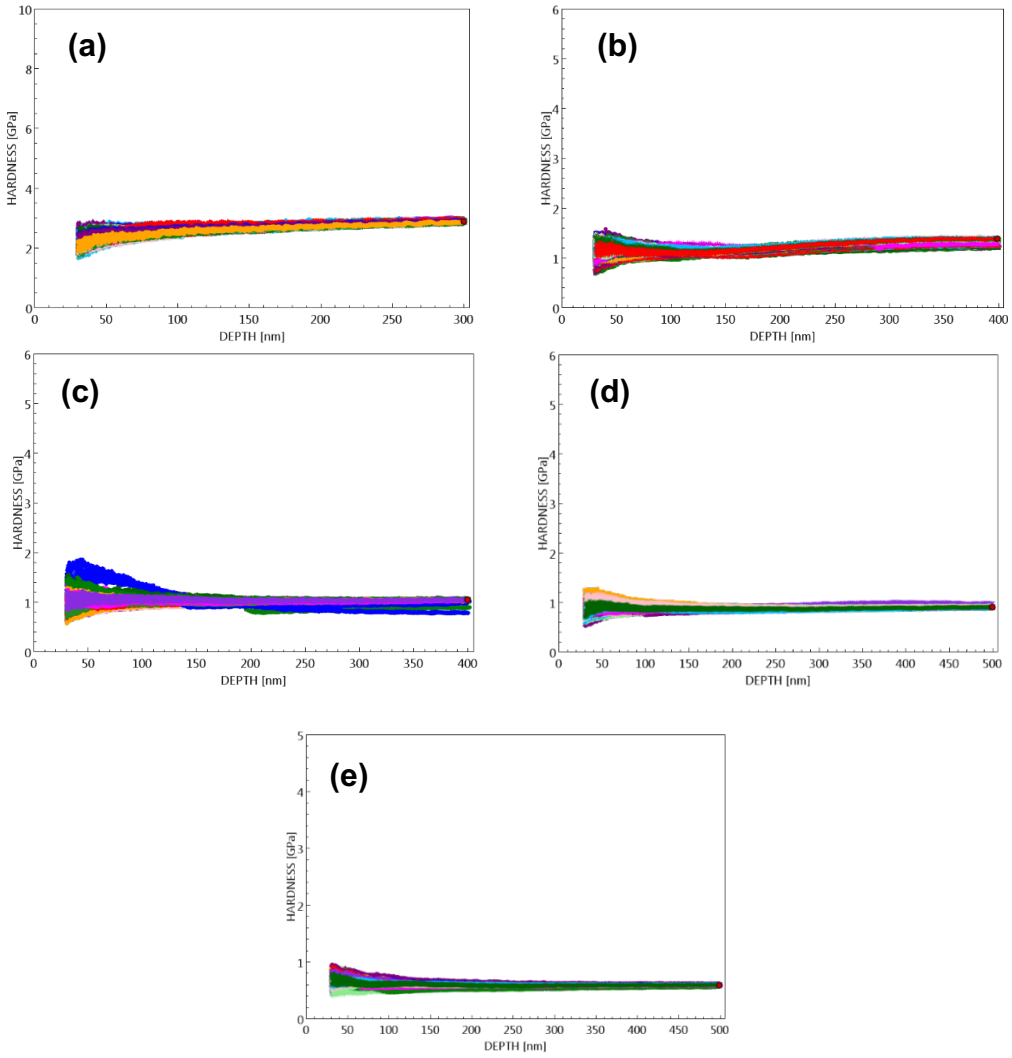

Figure S4. Hardness-depth curves of (a) full dense, (b) 40% of porosity, (c) 46% of porosity, (d) 51% of porosity, and (e) 59% of porosity thin film. Hardness data are relatively insensitive to depth, implying that there is no errors related to sink-in or pile-up.

Porosity	Young's modulus (GPa)	Hardness (GPa)
0	21.63 ± 0.2	2.91 ± 0.039
40	10.21 ± 0.2	1.295 ± 0.054
46	8.72 ± 0.36	1.037 ± 0.071
51	8.56 ± 0.13	0.908 ± 0.019
59	5.93 ± 0.07	0.597 ± 0.011

Table S3. Summary of nanoindentation data

3. Microcompression data of FIB-milled micropillars

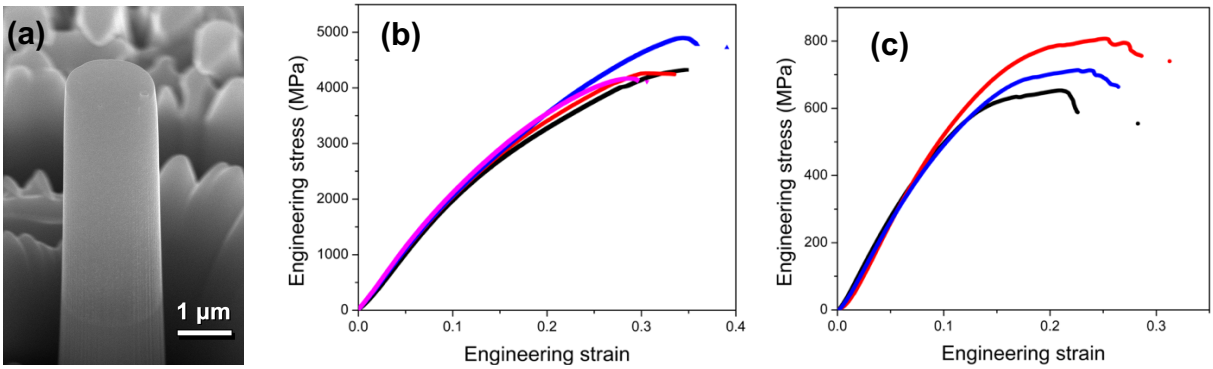

Figure S5. (a) SEM image of FIB-milled micropillar; Stress-strain curves of (b) full dense, (c) 59% of porosity FIB-milled micropillars with 2μm in diameter and 6μm in height. These pillars have about 260 times larger volume than nanoimprinted nanopillars, but their mechanical properties are nearly the same with those of nanoimprinted nanopillars. There is the weak size effect at the micrometer scale.

Porosity	Yield strength (MPa)		Fracture strength (MPa)		Fracture strain	
	FIB	Nanoimprint	FIB	Nanoimprint	FIB	Nanoimprint
0%	2661.41 ± 166.51	3121.68 ± 158.14	4372.70 ± 246.49	4198.53 ± 169.25	0.3338 ± 0.0236	0.3208 ± 0.0346
59%	511.75 ± 74.40	492.07 ± 55.80	673.31 ± 67.69	665.71 ± 38.00	0.2560 ± 0.0249	0.2456 ± 0.0113

Table S4. Summary of microcompression data of FIB-milled micropillars

4. Cyclic microcompression data

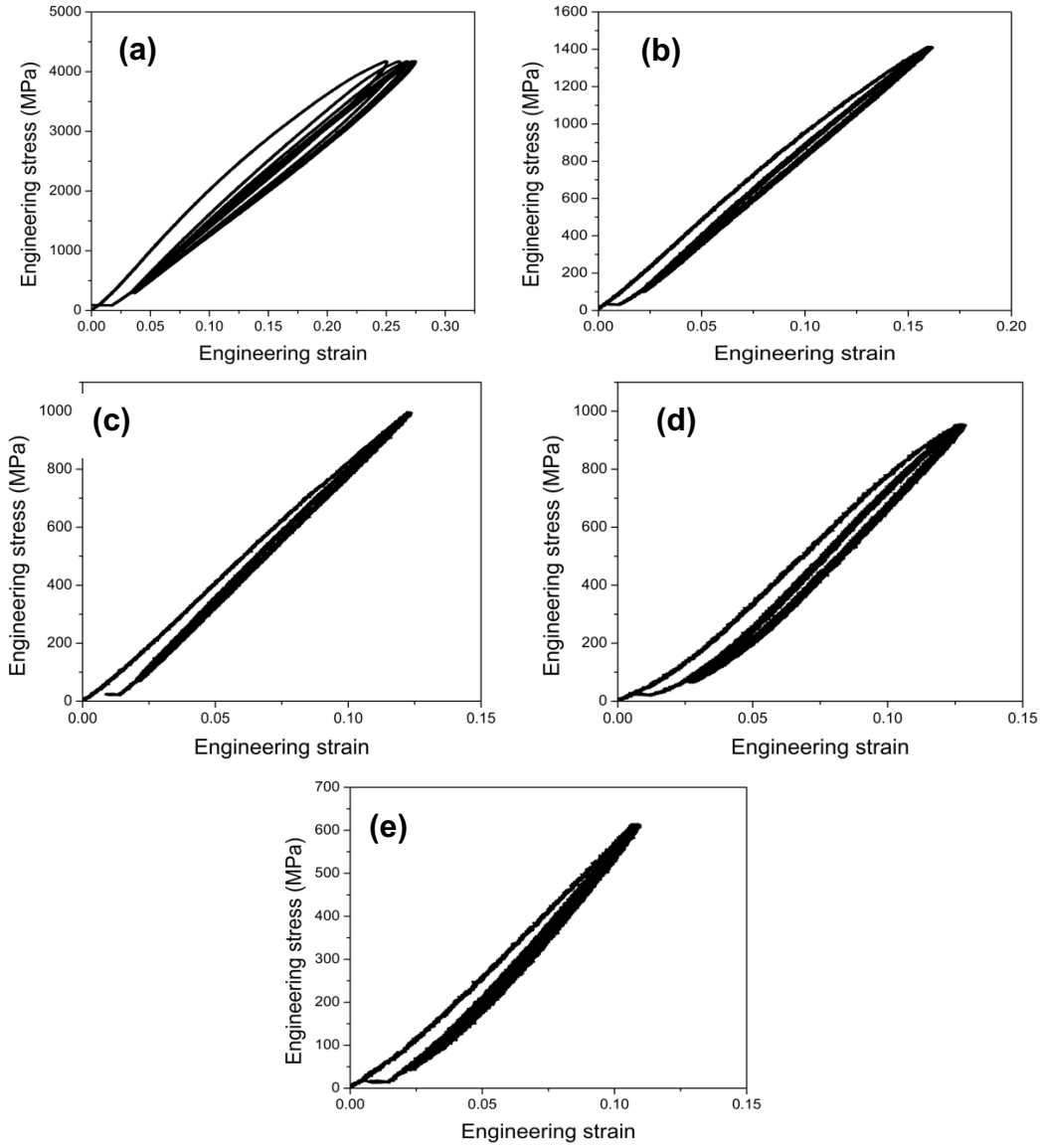

Figure S6. Stress-strain curves of (a) full dense, (b) 40% of porosity, (c) 46% of porosity, (d) 51% of porosity, and (e) 59% of porosity nanopillars.

Porosity	0%	40%	46%	51%	59%
Loss factor	0.0333 ± 0.0054	0.0172 ± 0.0025	0.0152 ± 0.0046	0.0244 ± 0.009	0.0203 ± 0.0071

Table S5. Summary of loss factor data

5. Synthesis of bulk-scale nanoporous amorphous carbon

Free standing nanoporous amorphous carbon was prepared following the procedure as described in the experimental section. Briefly, concentrated carbon precursor solution composed of PF resin and PDMS-b-PEO BBCP was drop casted in the fused silica mold with the dimension of 2cm by 1cm by 1cm. The carbon precursor was crosslinked at 140^{o}C for 4 hr in the nitrogen atmosphere followed by carbonization in conventional tube furnace in nitrogen atmosphere at 750^{o}C for 1hr with the heating rate of 10^{o}C/minute. After cooling down the system, nanoporous carbon was removed from the mold resulting in the preparation of free-standing carbon as shown in Figure S7.

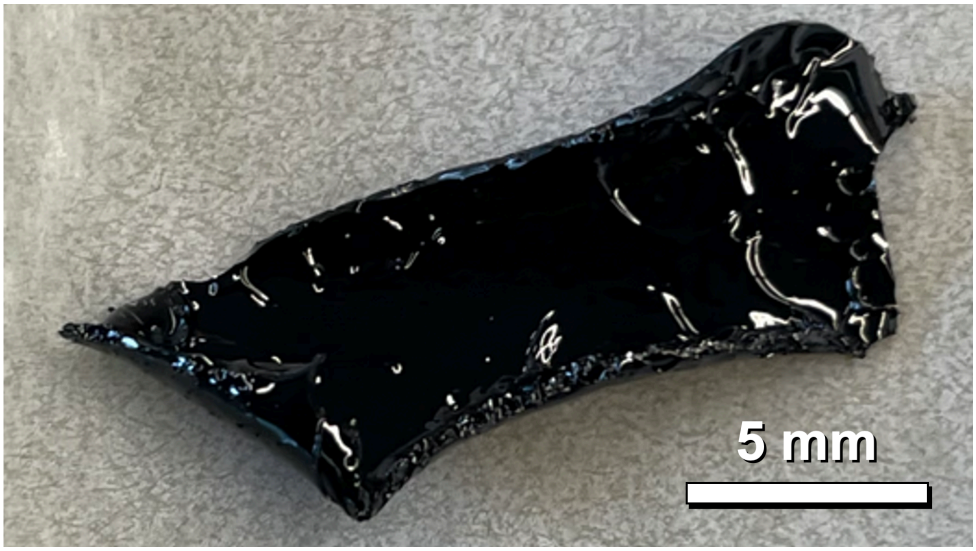

Figure S7. Optical image of free-standing nanoporous carbon with the dimension of 2cm by 0.5 cm.

6. Effect of strain rate on mechanical behavior: Atomistic Simulations

Atomic model for amorphous carbon

In this study, the amorphous carbon structures were generated employing two key methods: the liquid-quench method[2,3] and a reactive force field called ReaxFF[4]. The liquid quench method is particularly well-suited for effectively modeling amorphous behaviors, with a special focus on amorphous carbon[5–7], gels[8] and inorganic oxides[3]. ReaxFF, being a reactive potential, employs the concept of bond order to accurately model chemical interactions within a reactive system. By combining the liquid quench method with ReaxFF, we can proficiently simulate a diverse range of a-C structures spanning various densities.

The overall process of generating the model carbon structures, based on an experimental density of 1.6 g/cm^3, involves the following steps: (a) Start with 329,000 carbon atoms distributed randomly within a simulation cell measuring 155.2 × 155.2 × 155.2 nm^3, with fully periodic boundaries. (b) Ramp the temperature up to a high value of 10,000 K. (c) To avoid excessive overlap between the newly inserted atoms, maintain a minimum distance of 1.2 Å between any newly created atoms and the previously existing ones. (d) Allow the system to equilibrate at 10,000 K for 15 ps. (e) Rapidly cool down the system by quenching it to 4,000 K within 100 ps. (f) Conduct an annealing process at 4,000 K for 250 ps. Annealing involves controlled heating and slow cooling to reach a more stable state. (e) Quench the system to a lower temperature of 300 K, and then allow it to equilibrate at this temperature for approximately 10 ns.

During the equilibration runs, a fixed time step size of 0.2 fs was employed. Once the system reached an equilibrated configuration at 300 K, it was then utilized to investigate its mechanical properties. It is essential to emphasize that the temperature ranges chosen for the liquid quench simulations do not hold any direct physical significance[6,9,10]. Instead, they were selected

based on values commonly used in the scientific literature for similar studies. During the high-temperature equilibration stage at 10,000 K, the model carbon structures simulate a gas phase, where the carbon atoms are highly energetic and move freely, resembling a gas-like state.

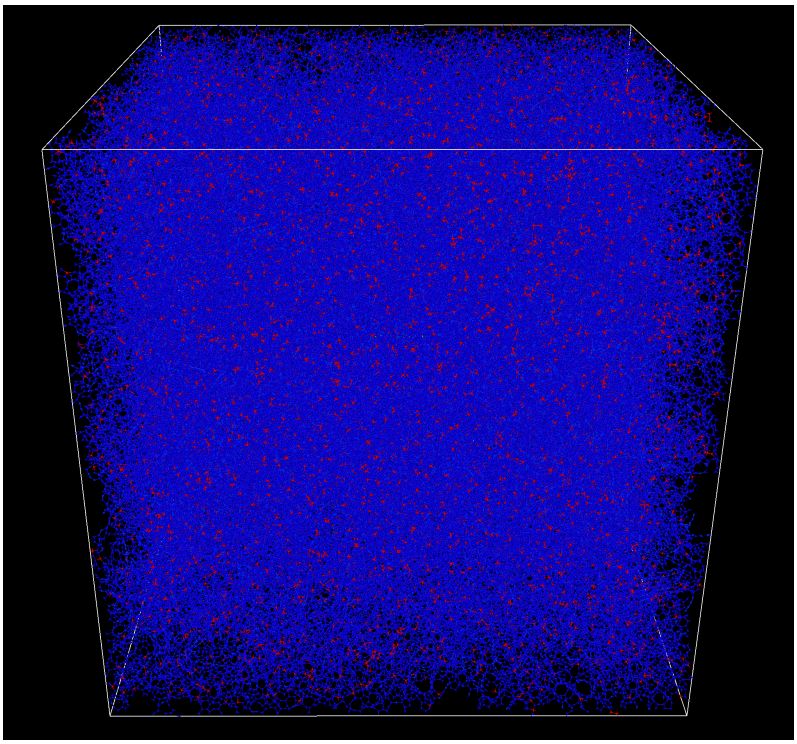

Figure S8. Initial structure of fully dense amorphous carbon with 1.6g/cm^3 of density. A red particle represents sp3-bonded carbon atom, and a blue particle represents sp2-bonded carbon atom.

MD simulations process for mechanical metrics

All molecular dynamics (MD) simulations in this study were performed using the Large-scale Atomic/Molecular Massively Parallel Simulator (LAMMPS) package[11]. Interaction potentials involving carbon particles are characterized by Adaptive Intermolecular Reactive Empirical Bond Order (AIREBO) Potential[12]. The AIREBO Potential is chosen because it provides

a highly accurate representation of the chemical interactions between carbon atoms, making it well-suited for capturing the chemistry and behavior of carbon-based materials in the simulations. This choice ensures the reliability and fidelity of the results obtained during the study.

After obtaining the equilibrium configuration, a relaxation time of 500 ps is further performed under the NPT ensemble at a constant temperature of 300 K and pressure of 0.0 MPa. Following the relaxation period, Non-Equilibrium Molecular Dynamics (NEMD) simulations are conducted to explore the system's response to stress-strain loading. In this NEMD simulation, the system is subjected to a stress-strain loading process by compressing it along the x-direction at a constant temperature of 300 K. The time step used for the NEMD simulation is 0.2 fs.

In the NEMD simulation, the x-dimension of the simulation box is systematically reduced during each loading stage using the $N\sigma_{ij}\varepsilon_{ij}T$ ensemble. During each loading stage, the system is subjected to a reduction in the x-dimension, effectively compressing the model carbon structures. The process continues until an approximate engineering compressive strain of 40% is achieved. During the loading process in the NEMD simulation, the system is constrained to maintain a pressure of 0 MPa along both the y and z directions. This constraint ensures that the dimensions along these two directions (y and z) are allowed to freely change as the x-dimension is compressed. This type of constraint is commonly used to simulate the Poisson's effect in materials.

Four different strain rates, including 5×10^{9} s^{-1}, 10^{9} s^{-1}, 5×10^{8} s^{-1}, and 10^{8} s^{-1}, are employed to investigate the strain rate effect on the material's mechanical behavior (Figure S9). During the loading process in the NEMD simulation, the carbon hybridization states (sp, sp2, and sp3) are computed based on the number of nearest neighbor carbon atoms within a cutoff radius of 2.0 Å.

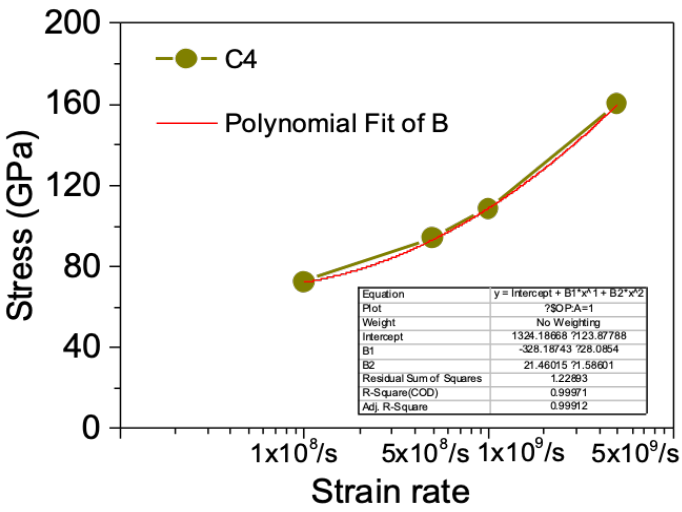

Figure S9. The effect of strain rate on yield strength

During the study, the researchers aim to explore the changes in the amorphous carbon configuration during the unloading process after reaching specific compressive strains under the compressive strain rate of 10^9 s^{-1}. After compressing the system to different compressive strains of 40% (with respect to the original length along the x-direction), the unloading process is initiated. During the unloading process, a tensile strain rate is applied to the x-direction until the compressive stress in the x-direction is close to zero. This means that the system is stretched along the x-direction to reverse the compression applied during the loading process. Exactly, after completing the loading and unloading processes and obtaining the stress-strain curves, the researchers can extract mechanical metrics such as the yield strength (σ_y) from the data. Additionally, during the loading and unloading processes, as mentioned earlier, carbon hybridization (sp, sp2, and sp3) is computed based on the number of nearest neighbor carbon atoms within a cutoff radius of 2.0 Å. By analyzing the carbon hybridization data at different stages of loading and unloading, the

researchers can study how the hybridization distribution changes under varying mechanical conditions.

Local curvature variation during compression

The enhancement of D peak intensity has been under debate for the past decades. The D peak intensity could increase when a crystal symmetry of graphite or graphene is broken by local disordering due to the creation of defects[13–15]. As discussed in main text, the local creation of sp3 bonds in the interior region of sp2 dominant structure could enhance the structural disordering, leading to the increase in D peak intensity. However, the creation of sp3 does not always increase the D peak intensity. If the sp2-to-sp3 transition occurs by destroying an aromatic ring or its partial structure, which are located at the edge of graphite or graphene structures, the D peak intensity could decrease[16]. Thus, the sp2-to-sp3 transition may not be able to change the D peak intensity for the small variation of sp2 (or sp3) content (in our case, only 4%).

Recent experimental studies showed that flattening carbon nanotube increases the D peak intensity dramatically[17]. They argue that the introduction of local curvature variation can enhance the D peak intensity a lot. Uniaxial compression could induce a similar topological change. If a slightly curved graphene-like structures in a nanopillar, uniaxial compression could fold such structure and increase the local curvature, enhancing the D peak intensity. Therefore, we searched for this kind of case from atomistic simulation.

Due to the high density of sp2 bonded atoms, amorphous carbon has many graphene-like monolayers. Because they are connected to neighboring carbon atom in a complex way, most of them are slightly distorted. We found that uniaxial compression could fold this structure more

severely and introduce the significant variation of local curvature (Figure S10, See also Supplementary Video), which can also be found from flattened carbon nanotube. Interestingly, this folding cannot be fully reversed, so highly curved structures could be maintained after full unloading. This could be the reason for the enhanced intensity of D peak in Raman spectroscopy data in compression pillar.

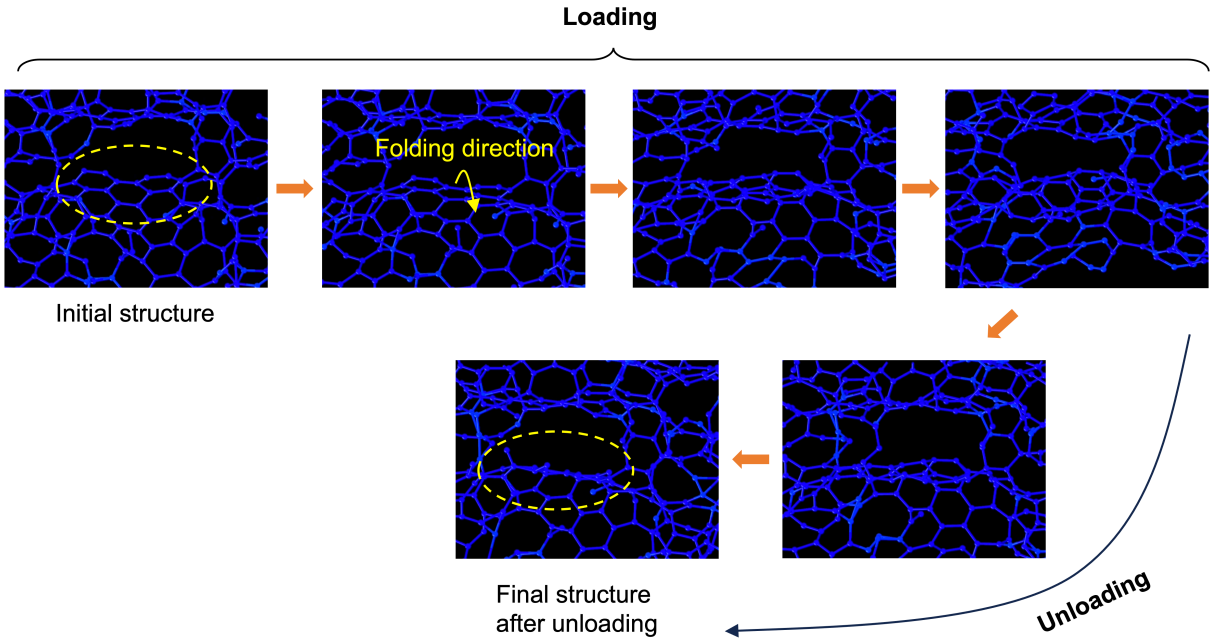

Figure S10. Simulation snapshot of local folding of sp2-bonded layer structure (See also Supplementary Video)

7. Ashby Chart

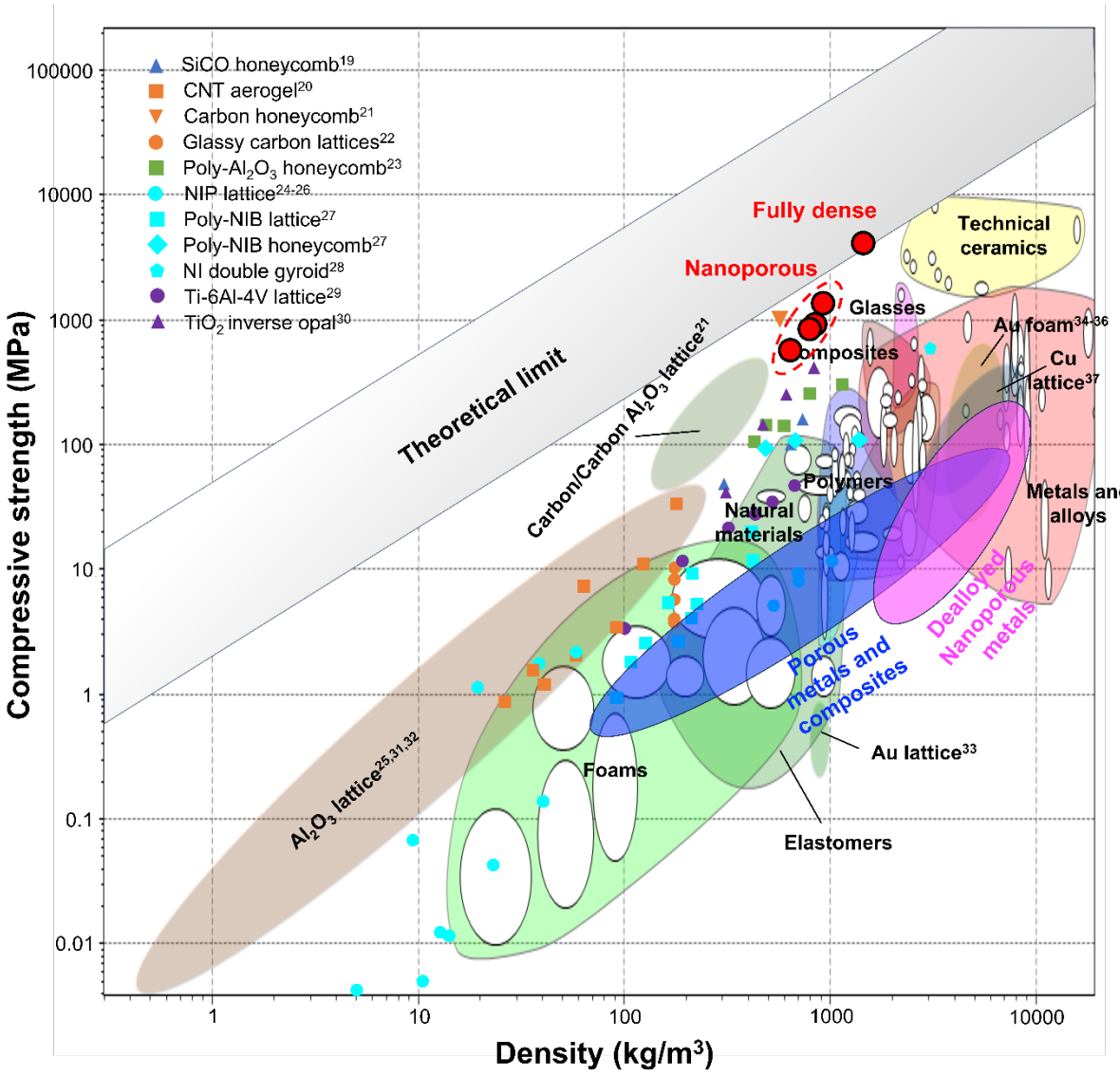

Figure S9. Compressive strength vs. density

All data have been obtained from the following references.

- Standard Ashby Chart[18]
- SiCO honeycomb[19]
- CNT aerogel[20]

- Carbon honeycomb[21]
- Carbon/Carbon Al_2O_3 lattice[21]
- Glassy carbon lattices[22]
- Poly-Al_2O_3 honeycomb[23]
- NIP lattice[24–26]
- Poly-NIB lattice[27]
- Poly-NIB honeycomb[27]
- NI double gyroid[28]
- Ti-6Al-4V lattice[29]
- TiO_2 inverse opal[30]
- Al_2O_3 lattice[25,31,32]
- Au lattice[33]
- Au foam[34–36]
- Cu lattice[37]

References

1. Ortel, E. *et al.* New approach on quantification of porosity of thin films via electron-excited X-ray spectra. *Anal Chem* 88, 7083–7090 (2016).
2. Galli, G., Martin, R. M., Car, R. & Parrinello, M. Structural and electronic properties of amorphous carbon. *Phys Rev Lett* 62, 555 (1989).
3. Rosen, J., Warschkow, O., McKenzie, D. R. & Bilek, M. M. M. Amorphous and crystalline phases in thermal quench simulations of alumina. *J Chem Phys* 126, (2007).
4. Van Duin, A. C. T., Dasgupta, S., Lorant, F. & Goddard, W. A. ReaxFF: a reactive force field for hydrocarbons. *J Phys Chem A* 105, 9396–9409 (2001).
5. Yu, J., Lucas, J., Wall, T., Liu, G. & Sheng, C. Modeling the development of char structure during the rapid heating of pulverized coal. *Combust Flame* 136, 519–532 (2004).
6. Suarez-Martinez, I. & Marks, N. A. Effect of microstructure on the thermal conductivity of disordered carbon. *Appl Phys Lett* 99, (2011).
7. Ranganathan, R., Rokkam, S., Desai, T. & Keblinski, P. Generation of amorphous carbon models using liquid quench method: A reactive molecular dynamics study. *Carbon N Y* 113, 87–99 (2017).
8. Bhattacharya, S. & Kieffer, J. Fractal dimensions of silica gels generated using reactive molecular dynamics simulations. *J Chem Phys* 122, (2005).
9. Palmer, J. C. *et al.* Modeling the structural evolution of carbide-derived carbons using quenched molecular dynamics. *Carbon N Y* 48, 1116–1123 (2010).
10. Shi, Y. A mimetic porous carbon model by quench molecular dynamics simulation. *J Chem Phys* 128, (2008).
11. Plimpton, S. Fast parallel algorithms for short-range molecular dynamics. *J Comput Phys* 117, 1–19 (1995).
12. Stuart, S. J., Tutein, A. B. & Harrison, J. A. A reactive potential for hydrocarbons with intermolecular interactions. *J Chem Phys* 112, 6472–6486 (2000).
13. Lucchese, M. M. *et al.* Quantifying ion-induced defects and Raman relaxation length in graphene. *Carbon N Y* 48, 1592–1597 (2010).
14. Eckmann, A. *et al.* Probing the nature of defects in graphene by Raman spectroscopy. *Nano Lett* 12, 3925–3930 (2012).
15. Cançado, L. G. *et al.* Disentangling contributions of point and line defects in the Raman spectra of graphene-related materials. *2d Mater* 4, 025039 (2017).
16. Ferrari, A. C. & Robertson, J. Interpretation of Raman spectra of disordered and amorphous carbon. *Phys Rev B* 61, 14095 (2000).
17. Picheau, E. *et al.* Intense Raman D Band without Disorder in Flattened Carbon Nanotubes. *ACS Nano* 15, 596–603 (2021).
18. Ashby, M. F. *Materials Selection in Mechanical Design*. (Elsevier Science, 2016).
19. Eckel, Z. C. *et al.* Additive manufacturing of polymer-derived ceramics. *Science (1979)* 351, 58–62 (2016).
20. Shin, S. J., Kucheyev, S. O., Worsley, M. A. & Hamza, A. V. Mechanical deformation of carbon-nanotube-based aerogels. *Carbon N Y* 50, 5340–5342 (2012).

21. Bauer, J., Schroer, A., Schwaiger, R. & Kraft, O. Approaching theoretical strength in glassy carbon nanolattices. *Nat Mater* 15, 438–443 (2016).
22. Jacobsen, A. J., Mahoney, S., Carter, W. B. & Nutt, S. Vitreous carbon micro-lattice structures. *Carbon N Y* 49, 1025–1032 (2011).
23. Bauer, J., Hengsbach, S., Tesari, I., Schwaiger, R. & Kraft, O. High-strength cellular ceramic composites with 3D microarchitecture. *Proceedings of the National Academy of Sciences* 111, 2453–2458 (2014).
24. Valdevit, L., Godfrey, S. W., Schaedler, T. A., Jacobsen, A. J. & Carter, W. B. Compressive strength of hollow microlattices: Experimental characterization, modeling, and optimal design. *J Mater Res* 28, 2461–2473 (2013).
25. Zheng, X. *et al.* Ultralight, ultrastiff mechanical metamaterials. *Science (1979)* 344, 1373–1377 (2014).
26. Torrents, A., Schaedler, T. A., Jacobsen, A. J., Carter, W. B. & Valdevit, L. Characterization of nickel-based microlattice materials with structural hierarchy from the nanometer to the millimeter scale. *Acta Mater* 60, 3511–3523 (2012).
27. Mieszala, M. *et al.* Micromechanics of amorphous metal/polymer hybrid structures with 3D cellular architectures: size effects, buckling behavior, and energy absorption capability. *Small* 13, 1602514 (2017).
28. Khaderi, S. N. *et al.* The indentation response of Nickel nano double gyroid lattices. *Extreme Mech Lett* 10, 15–23 (2017).
29. Dong, L., Deshpande, V. & Wadley, H. Mechanical response of Ti–6Al–4V octet-truss lattice structures. *Int J Solids Struct* 60, 107–124 (2015).
30. do Rosário, J. J., Berger, J. B., Lilleodden, E. T., McMeeking, R. M. & Schneider, G. A. The stiffness and strength of metamaterials based on the inverse opal architecture. *Extreme Mech Lett* 12, 86–96 (2017).
31. Meza, L. R., Das, S. & Greer, J. R. Strong, lightweight, and recoverable three-dimensional ceramic nanolattices. *Science (1979)* 345, 1322–1326 (2014).
32. Meza, L. R. *et al.* Resilient 3D hierarchical architected metamaterials. *Proceedings of the National Academy of Sciences* 112, 11502–11507 (2015).
33. Montemayor, L. C. & Greer, J. R. Mechanical response of hollow metallic nanolattices: combining structural and material size effects. *J Appl Mech* 82, 071012 (2015).
34. Volkert, C. A., Lilleodden, E. T., Kramer, D. & Weissmüller, J. Approaching the theoretical strength in nanoporous Au. *Appl Phys Lett* 89, (2006).
35. Biener, J., Hodge, A. M., Hamza, A. V, Hsiung, L. M. & Satcher, J. H. Nanoporous Au: A high yield strength material. *J Appl Phys* 97, (2005).
36. Hodge, A. M. *et al.* Scaling equation for yield strength of nanoporous open-cell foams. *Acta Mater* 55, 1343–1349 (2007).
37. Gu, X. W. & Greer, J. R. Ultra-strong architected Cu meso-lattices. *Extreme Mech Lett* 2, 7–14 (2015).